Journal of Applied Physics

RESEARCH ARTICLE | MARCH 14 2023

An electromagnetic scattering approach to identifying topological and non-topological unidirectional edge states at gyrotropic plasma interfaces

Hossein Mehrpour Bernety ; Mark A. Cappelli

Journal of Applied Physics 133, 104902 (2023)
https://doi.org/10.1063/5.0124165

Journal of Applied Physics ARTICLE scitation.org/journal/jap

An electromagnetic scattering approach to identifying topological and non-topological unidirectional edge states at gyrotropic plasma interfaces

Cite as: J. Appl. Phys. **133**, 104902 (2023); doi: 10.1063/5.0124165
Submitted: 3 September 2022 · Accepted: 23 February 2023 ·
Published Online: 14 March 2023

Hossein Mehrpour Bernety[a] and Mark A. Cappelli

AFFILIATIONS

Department of Mechanical Engineering, Stanford University, Stanford, California 94305, USA

[a]**Author to whom correspondence should be addressed:** bernety@stanford.edu

ABSTRACT

We present an approach to identifying topological edge states in two dimensional (2D) problems. Such scattering-immune surface waves are typically identified using the Berry concept, which evaluates Chern numbers of bulk transmission bands. Instead, here, we approach the task from an analytical electromagnetic scattering perspective, which enables the study of a wide class of configurations in which waves are confined to propagate at the interface between a topologically non-trivial magnetized plasma and a topologically trivial medium such as air. Although it is of theoretical significance to classify interfacial states by their topological invariants, we believe that this approach enables the engagement of a broader range of researchers, particularly experimentalists who seek to design devices that exploit the ensuing non-reciprocal and scattering-immune properties.

I. INTRODUCTION

The propagation of electromagnetic waves in linear time-invariant (LTI) systems[1] is constrained by the Lorentz reciprocity.[2] The constitutive parameters of materials comprising such a system can be expressed as a symmetric tensor,[3] i.e., the positions of an electromagnetic source (such as a transmitting antenna) and a receiver (a receiving antenna) can be interchanged without affecting their readings, reflecting the symmetry in their scattering matrices.[4,5] Breaking this symmetry and, consequently, achieving non-reciprocity, is of interest for designing various devices such as one-way waveguides, isolators, and circulators, among others. To achieve non-reciprocity, one may follow various approaches[6] such as the introduction of a non-linearity[7] or time modulation.[8,9] In the case of a magnetizable medium, the application of a magnetic bias breaks this symmetry by introducing anisotropy in either the magnetic permeability or dielectric permittivity.[10–13] Kord *et al.*[6] provides a review of these various fundamental approaches that are used to break such time-reversal symmetry.

As the fundamental physics enabling the breaking of time-reversal symmetry is unraveled, we are seeing an increased interest in the identification of new materials and technologies for use in developing practical devices for the manipulation or control of electromagnetic (EM) waves. Metamaterials and photonic crystals, which fall within a class of engineered materials, have provided great opportunities in this regard, leading to applications in communications and wireless sensing, among others. Within the bandgap of a bulk medium constructed from such engineered materials, the propagation of EM waves is forbidden, and as a result, the material behaves as an EM insulator. Recently, new physics has emerged from the understanding of what happens in classes of electromagnetically insulating materials when the symmetry of such bulk materials is broken at an interface. Those that fall within the class of so-called topologically non-trivial materials or "topological insulators"[14] give rise to non-reciprocal propagation of interfacial states that are immune to scattering from surface irregularities.[15–28] Non-reciprocal interfacial states that exhibit such robust immunity to scattering are said to be "topologically protected." These states reside within and span across the bulk bands defining the gap. The topological classification of these bulk bands is achieved by computing the Berry phase, which, when integrated

across momentum (k) space determines the so-called band Chern number, C_n, an integer value describing the winding of the field polarization across momentum space.[16,29] The topology of the gap is classified by the "gap Chern number," $C_{i,j}$ which is the sum of all band Chern numbers with $n \leq i$, i.e., below the gap.[29] When topologically non-trivial insulators (characterized by a non-zero gap Chern number) share an interface with a medium having an overlapping bandgap but of a differing gap Chern number), non-reciprocal and scattering-immune edge states may emerge.[19] The difference between the gap Chern numbers of the two mediums define the number of interfacial or "edge" states in accordance with the bulk-edge correspondence principle.[30] As an example, a medium with a gap Chern number of 1, in contact with a metal, which has a gap Chern number of zero, will support one such scattering-immune interfacial states. In contrast, the same non-trivial medium in contact with a dielectric such as air, which is also trivial in its topology, does not support true topologically protected edge states because it is not electromagnetically insulating even though in some cases supported waves can be strongly unidirectional.[31]

This topological classification provides a convenient way of identifying possible material pairs that may support these scattering-immune non-reciprocal modes in gapped insulators when band Chern numbers can be easily computed. However, it should be noted that one-way surface waves have been explored long before[32,33] their topological classification, i.e., well before the discovery of Chern invariants and the Berry phase concepts.[16,34] Furthermore, many interfacial modes, such as surface plasmon polaritons (SPPs), also referred to as magnetoplasmons, at the interface of plasmonic materials[31] and dielectrics propagate below the plasmonic gap. In this paper, we describe a classical scattering approach to study the possible propagation of interfacial states at the boundary between a gyrotropic, magnetized bulk plasma and a medium such as a dielectric (e.g., air or vacuum) or metal. We believe that this approach can serve as an alternate tool that enables experimentalists to evaluate the robustness of configurations and conditions that exhibit the support of non-reciprocal interfacial states. The approach described here identifies the topological modes through their main electromagnetic characteristics, instead of determining their topological indices. We extend this tool to identify such states in more complex configurations, such as plasma metamaterials (a collection or array of plasma elements), where computing the Chern numbers of such effective mediums may be more cumbersome. Our particular interest in the use of magnetized plasmas is through the opportunities that they present in the reconfigurability (e.g., tuning) of such systems. Examples are provided to illustrate the broad utility of the approach, in particular, for cases and configurations that involve experimentally realizable plasma-based systems comprising columnar plasma discharge tubes. In Sec. II, we introduce our analytical formulation of the 2D problem. In Sec. III, we show how one can investigate the presence of interfacial states using this analytical formulation, particularly two strongly unidirectional states in two-dimensional (2D) EM wave propagation in the so-called Voigt configuration, where the propagation is orthogonal to the imposed z-directed magnetic bias with transverse-electric (TE^z) polarization. In Sec. IV, we provide a brief interpretation of the results within the context of topological classifications. Section V summarizes our work and offers conclusions.

II. ANALYTICAL FORMULATION

Here, we consider the 2D problem incorporating the presence of a magnetic line source (to excite TE^z waves), located at radial and azimuthal positions ($\rho = \rho'$, $\varphi = \varphi'$), within a region sandwiched between a uniform gyrotropic bulk plasma modeled by a cylinder with a radius of r_p ($\rho < r_p$), and an isotropic "cladding" material of inner radius, r_c ($\rho > r_c$), extending to the arbitrary large radius, as shown in Fig. 1. The region, or gap between the plasma and the cladding, can be a dielectric such as air, or even vacuum, with a unity dielectric constant. The plasma is biased with a static magnetic field that points along the z-direction.

A. Fields from the magnetic line source

The magnetic field generated by the magnetic line source, I_m, positioned within the gap, $\mathbf{H}^i$, can be expressed as an infinite series summation of cylindrical wave functions,[5]

$$\mathbf{H}^i = \hat{\mathbf{z}} H_z^i = \hat{\mathbf{z}} H_0 \begin{cases} \sum_{n=-\infty}^{\infty} J_n(k_0\rho) H_n^{(2)}(k_0\rho') e^{jn(\varphi-\varphi')}; \; r_p < \rho < \rho' \\ \sum_{n=-\infty}^{\infty} J_n(k_0\rho') H_n^{(2)}(k_0\rho) e^{jn(\varphi-\varphi')}; \; r_c > \rho > \rho' \end{cases}. \tag{1a}$$

where k_0 represents the free space wave number, H_0 is the

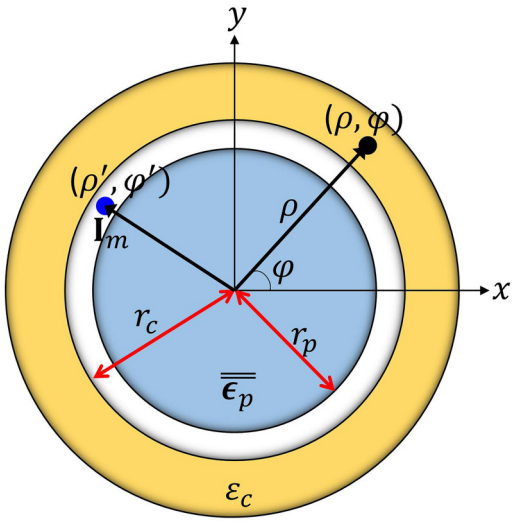

FIG. 1. Schematic of the configuration used to investigate edge states in a 2D problem. A magnetic line source (I_m) is positioned in an un-ionized gap (white region) between a magnetized plasma (shown in light blue) characterized by an anisotropic relative permittivity tensor, $\bar{\bar{\varepsilon}}_p$, and an isotropic "cladding" of dielectric constant (shown in yellow), ε_c.

amplitude of the magnetic field

$$H_0 = -\frac{k_0^2 I_m}{4\omega\mu_0}, \tag{1b}$$

J_n is the Bessel function of the first kind, and $H_n^{(2)}$ is the Hankel function of the second kind. The incident electric field, $\mathbf{E}^i$, can then be written as

$$\mathbf{E}^i = \frac{1}{j\omega\varepsilon_0}\nabla\times\mathbf{H}^i = E_\rho^i\hat{\rho} + E_\varphi^i\hat{\varphi}, \tag{2a}$$

where

$$E_\rho^i = \frac{H_0}{j\omega\varepsilon_0\rho}\begin{cases}\sum_{n=-\infty}^{\infty} jnJ_n(k_0\rho)H_n^{(2)}(k_0\rho')e^{jn(\varphi-\varphi')}; r_p<\rho<\rho'\\ \sum_{n=-\infty}^{\infty} jnJ_n(k_0\rho')H_n^{(2)}(k_0\rho)e^{jn(\varphi-\varphi')}; r_c>\rho>\rho'\end{cases}, \tag{2b}$$

$$E_\varphi^i = \frac{-H_0}{j\omega\varepsilon_0}\begin{cases}\sum_{n=-\infty}^{\infty} J_n'(k_0\rho)H_n^{(2)}(k_0\rho')e^{jn(\varphi-\varphi')}; r_p<\rho<\rho'\\ \sum_{n=-\infty}^{\infty} J_n(k_0\rho')H_n^{(2)'}(k_0\rho)e^{jn(\varphi-\varphi')}; r_c>\rho>\rho'\end{cases}, \tag{2c}$$

and

$$J_n'(k_0\rho) = \frac{\partial J_n(k_0\rho)}{\partial\rho}; \quad k_0 = 2\pi f\sqrt{\varepsilon_0\mu_0}, \tag{3a}$$

$$H_n^{(2)'}(k_0\rho) = \frac{\partial H_n^{(2)}(k_0\rho)}{\partial\rho}, \tag{3b}$$

which can be evaluated using the relation

$$J_n'(\alpha x) = \frac{\partial J_n(\alpha x)}{\partial x} = \alpha J_{n-1}(\alpha x) - \frac{n}{x}J_n(\alpha x), \tag{3c}$$

$$H_n^{(2)'}(\alpha x) = \frac{\partial H_n^{(2)}(\alpha x)}{\partial x} = \alpha H_{n-1}^{(2)}(\alpha x) - \frac{n}{x}H_n^{(2)}(\alpha x). \tag{3d}$$

B. Scattered fields in the isotropic cladding

We can express the magnetic and electric fields that are scattered into the cladding medium, $\mathbf{H}^c$ and $\mathbf{E}^c$, as

$$\mathbf{H}^c = \hat{\mathbf{z}}H_z^c = \hat{\mathbf{z}}\sum_{n=-\infty}^{\infty} a_n H_n^{(2)}(k_c\rho)e^{jn(\varphi-\varphi')}, \tag{4}$$

$$\mathbf{E}^c = \frac{1}{j\omega\varepsilon_0\varepsilon_c}\nabla\times\mathbf{H}^c = E_\rho^c\hat{\rho} + E_\varphi^c\hat{\varphi}, \tag{5a}$$

with

$$E_\rho^c = \frac{1}{j\omega\varepsilon_0\varepsilon_c\rho}\sum_{n=-\infty}^{\infty} jna_n H_n^{(2)}(k_c\rho)e^{jn(\varphi-\varphi')}, \tag{5b}$$

$$E_\varphi^c = \frac{-1}{j\omega\varepsilon_0\varepsilon_c}\sum_{n=-\infty}^{\infty} a_n H_n^{(2)'}(k_c\rho)e^{jn(\varphi-\varphi')}. \tag{5c}$$

C. Scattered fields in the gap

The scattered fields inside the gap ($\mathbf{E}^a$ and $\mathbf{H}^a$) are represented as

$$\mathbf{H}^a = \hat{\mathbf{z}}\sum_{n=-\infty}^{\infty}[B_nJ_n(k_0\rho) + C_nY_n(k_0\rho)]e^{jn(\varphi-\varphi')}, \tag{6}$$

$$\mathbf{E}^a = \frac{1}{j\omega\varepsilon_0}\nabla\times\mathbf{H}^a = E_\rho^a\hat{\rho} + E_\varphi^a\hat{\varphi}, \tag{7a}$$

where

$$E_\rho^a = \frac{1}{j\omega\varepsilon_0\rho}\sum_{n=-\infty}^{\infty} jn[B_nJ_n(k_0\rho) + C_nY_n(k_0\rho)]e^{jn(\varphi-\varphi')}, \tag{7b}$$

$$E_\varphi^a = \frac{-1}{j\omega\varepsilon_0}\sum_{n=-\infty}^{\infty}\left[B_nJ_n'(k_0\rho) + C_nY_n'(k_0\rho)\right]e^{jn(\varphi-\varphi')}. \tag{7c}$$

D. Penetrated fields in the bulk magnetized plasma

Finally, the fields inside the magnetized plasma ($\mathbf{E}^p$ and $\mathbf{H}^p$) with a relative permittivity tensor, $\bar{\bar{\varepsilon}}_p$, given by

$$\bar{\bar{\varepsilon}}_p = \begin{bmatrix}\varepsilon_t & j\varepsilon_g & 0\\ -j\varepsilon_g & \varepsilon_t & 0\\ 0 & 0 & \varepsilon_z\end{bmatrix} \tag{8}$$

can be expressed as

$$\mathbf{H}^p = \hat{\mathbf{z}}H_z^p = \hat{\mathbf{z}}\sum_{n=-\infty}^{\infty} d_nJ_n(k_p\rho)e^{jn(\varphi-\varphi')}, \tag{9}$$

$$\mathbf{E}^p = \frac{1}{j\omega\varepsilon_0}\bar{\bar{\varepsilon}}_p^{-1}\cdot(\nabla\times\mathbf{H}^p) = E_\rho^p\hat{\rho} + E_\varphi^p\hat{\varphi}, \tag{10a}$$

where

$$E_\rho^p = \frac{1}{j\omega\varepsilon_0\rho}\frac{1}{\varepsilon_p}\left[\sum_{n=-\infty}^{\infty} jnd_nJ_n(k_p\rho)e^{jn(\varphi-\varphi')}\right] + \frac{1}{j\omega\varepsilon_0}\frac{j}{\varepsilon_p'}\left[\sum_{n=-\infty}^{\infty} d_nJ_n'(k_p\rho)e^{jn(\varphi-\varphi')}\right], \tag{10b}$$

$$E_\varphi^p = \frac{1}{j\omega\varepsilon_0\rho}\frac{j}{\varepsilon_p'}\left[\sum_{n=-\infty}^{\infty} jnd_nJ_n(k_p\rho)e^{jn(\varphi-\varphi')}\right] - \frac{1}{j\omega\varepsilon_0}\frac{1}{\varepsilon_p}\left[\sum_{n=-\infty}^{\infty} d_nJ_n'(k_p\rho)e^{jn(\varphi-\varphi')}\right]. \tag{10c}$$

The elements of $\overline{\overline{\epsilon}}_p$ are

$$\varepsilon_t = 1 - \frac{\omega_p^2(\omega - j\nu_c)}{\omega[(\omega - j\nu_c)^2 - \omega_b^2]}, \tag{11a}$$

$$\varepsilon_g = -\frac{\omega_p^2\omega_b}{\omega[(\omega - j\nu_c)^2 - \omega_b^2]}, \tag{11b}$$

$$\varepsilon_z = 1 - \frac{\omega_p^2}{\omega(\omega - j\nu_c)}. \tag{11c}$$

Here, $\omega_p = 2\pi f_p$, $\omega_b = 2\pi f_b$, and $\omega = 2\pi f$ are the plasma, cyclotron, and field frequencies in rad/s, respectively, and the wave damping due to electron scattering with the background plasma gas is denoted by ν_c in Hz. The inverse of the relative permittivity tensor can be expressed as

$$\overline{\overline{\epsilon}}_p^{-1} = \begin{bmatrix} \frac{\varepsilon_t}{\varepsilon_t^2-\varepsilon_g^2} & \frac{-j\varepsilon_g}{\varepsilon_t^2-\varepsilon_g^2} & 0 \\ \frac{j\varepsilon_g}{\varepsilon_t^2-\varepsilon_g^2} & \frac{\varepsilon_t}{\varepsilon_t^2-\varepsilon_g^2} & 0 \\ 0 & 0 & \frac{1}{\varepsilon_z} \end{bmatrix} = \begin{bmatrix} \frac{1}{\varepsilon_p} & \frac{-j}{\varepsilon_p'} & 0 \\ \frac{j}{\varepsilon_p'} & \frac{1}{\varepsilon_p} & 0 \\ 0 & 0 & \frac{1}{\varepsilon_z} \end{bmatrix}. \tag{12}$$

Accordingly, the permittivity seen by the penetrated fields for the gyrotropic cylinder will be

$$\varepsilon_p = \frac{\varepsilon_t^2 - \varepsilon_g^2}{\varepsilon_t} \rightarrow k_p = k_0\sqrt{\varepsilon_p}. \tag{13}$$

Also, we define

$$\varepsilon_p' = \frac{\varepsilon_t^2 - \varepsilon_g^2}{\varepsilon_g}. \tag{14}$$

To solve for all unknown expansion coefficients a_n, B_n, C_n, and d_n, one applies the corresponding boundary conditions that enforce the continuity of tangential electric and magnetic fields at $\rho = r_p$ and $\rho = r_c$. The details are given in the Appendix.

III. POSSIBLE INTERFACIAL STATES

In this section, we apply the above electromagnetic formalism to search for possible robust, unidirectional interfacial states. As described below, we introduce a merit function and survey conditions for the magnetic field and wave frequency in a given bulk plasma configuration to identify regimes over which such states may be excited.

A. Merit function

For a bulk, non-magnetized plasma, the excitation of a magnetic line source at an azimuthal location within the un-ionized gap, $\varphi' = 180°$, leads to a symmetric propagation of power, i.e., the power has no preferred direction of propagation on either side of the x–y plane. Such a behavior is expected regardless of the plasma collisionality, ν_c. However, by applying a magnetic field along the axis of the plasma column (i.e., z-axis), this symmetry can be broken. In this regard, to achieve unidirectional interfacial modes using the magnetic line excitation, the fields need to be directed through either Path I or Path II as shown in Fig. 2.

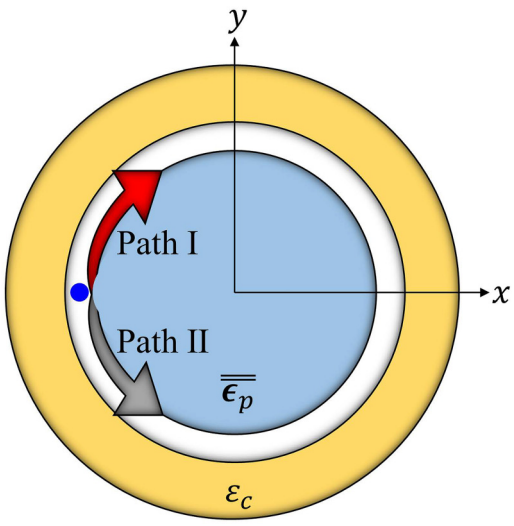

FIG. 2. Possible paths for topological surface waves.

In general, one can use various strategies with a range of mathematical objective functions to determine the conditions required to identify plasma density and magnetic field conditions that lead to strongly confined unidirectional surface modes within this un-ionized gap. Here, we present a simple and realizable criterion to find such modes. Without loss of generality, we assume that the magnetic line source is located at $r_p < \rho' < r_c$ and $\varphi' = 180°$.

We seek to find values of f/f_p and f_b/f_p such that the magnitude of the wave magnetic field (H-field) along Path II is significantly greater than that of the field along Path I (or, vice versa). We note, however, that in the case of no collisionality, for this geometry, the magnitude of the magnetic field will be independent of the azimuthal location and conditions will appear symmetric as we examine only the quasi-steady state behavior. Some level of collisional damping (i.e., a finite value of ν_c), therefore, facilitates the identification of unidirectional propagation.

For any particular excitation frequency, we define a merit function, F, as

$$F(f, f_b, f_p) = \frac{S^{II}}{S^I + S^a + S^p}, \tag{15}$$

wherein

$$S^I = \int_0^{\pi}\int_{r_p-\Delta_r}^{r_p+\Delta_r} |H_z(\rho, \varphi)|^2\, \rho\, d\rho\, d\varphi, \tag{16a}$$

$$S^{II} = \int_{\pi}^{2\pi}\int_{r_p-\Delta_r}^{r_p+\Delta_r} |H_z(\rho, \varphi)|^2\, \rho\, d\rho\, d\varphi, \tag{16b}$$

$$S^a = \int_0^{2\pi} \int_{r_p+\Delta_r}^{r_c} |H_z^a(\rho, \varphi) + H_z^i(\rho, \varphi)|^2 \, \rho \, d\rho \, d\varphi, \tag{16c}$$

$$S^p = \int_0^{2\pi} \int_0^{r_p-\Delta_r} |H_z^p(\rho, \varphi)|^2 \, \rho \, d\rho \, d\varphi. \tag{16d}$$

This merit function describes the ratio of the power focused at the edge of the magnetized plasma cylinder on Path II (S^{II}) to the sum of the power that penetrates into the magnetized plasma cylinder (S^p), the power in the air gap (S^a), and the focused power on Path I (S^I). One can also normalize it to its respective maximum and present it in decibels (dB) as follows:

$$F_{dB}^{\text{norm}} = 10 \log_{10}\left(\frac{F}{F_{\max}}\right). \tag{17}$$

If there exists a possible interfacial wave for specific values of f, f_b, and f_p, the merit function should attain a strong maximum at those values. In determining optimum conditions we survey the landscape of relative field frequency, f/f_p, and relative cyclotron frequency, f_b/f_p, for a particular geometry, collisionality, and cladding material property. To facilitate the survey we sweep the magnetic field from negative to positive values, which delineates the direction of propagation of the identified modes. We consider the plasma radius to be $r_p = 60$ mm. We assume an achievable plasma frequency of $f_p = 6.3$ GHz and a nominal value of $\nu_c \approx 0.16 f_p = 1$ GHz, unless otherwise stated, in our analysis. This geometry and these conditions are realizable in the laboratory with low pressure gas discharge devices, in this case, particularly magnetized plasmas generated in helicon discharge sources.[35]

B. Air cladding: Unidirectional, non-topological surface waves

Here, we first consider a topologically trivial cladding such as air (or its electromagnetic equivalent, vacuum, or any un-ionized gas, with a unity scalar dielectric constant), representing the case of a uniform magnetized plasma-vacuum (or plasma-un-ionized gas) boundary. We consider two different source locations: (a) $\rho' = 65$ mm and (b) $\rho' = 61$ mm. Equivalently, the distance between the source and the magnetized plasma rod is 5 and 1 mm, for cases (a) and (b), respectively. The respective merit functions are shown in Fig. 3. The region of strong activity (red shaded region) below the plasma frequency in Fig. 3(a), which is also present in Fig. 3(b), refers to the unidirectional magnetized SPP or Voigt-configured magnetoplasmon waves. These surface waves are immune to backscattering,[36] but, as mentioned earlier, they are non-topological in their classification.[37] In the absence of a magnetic field, these disturbances are slow waves, propagating at less than the speed of EM waves in the adjacent dielectric and bidirectional in their dispersion, with a resonance at $f_r = f_p/\sqrt{2}$ (when air or vacuum is the clad material). The presence of an external magnetic bias breaks the directional symmetry, introducing a unidirectional gap that spans between frequencies of $f_r^{\pm} = f_r \pm f_b/2$. Apparent in Fig. 3 for both locations of the source is that for this magnetoplasmon disturbance, the strength of the coupling to the

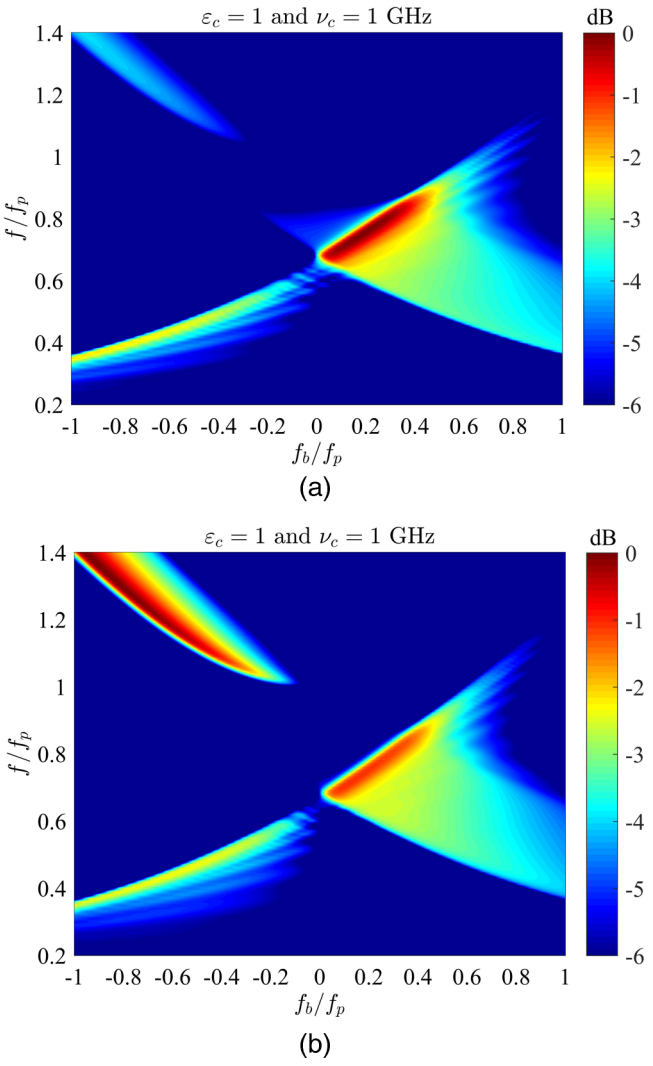

FIG. 3. The merit function normalized to its maximum in dB, F_{dB}^{norm}, vs f_b/f_p and f/f_p, for $\varepsilon_c = 1$ (such as an un-ionized gas as the cladding medium) and $\nu_c = 1$ GHz: (a) $\rho' = 65$ mm and (b) $\rho' = 61$ mm.

surface wave is greater at the top of the unidirectional band, closer to the upper resonance, as seen in recent simulations carried out by Pakniyat *et al.*[37]

The wave magnetic field magnitude's distribution around the plasma cylinder for this low frequency mode for the specific case of $f/f_p = 0.78$ and $f_b/f_p = 0.24$ is shown in Fig. 4 for two values of the collision frequency, $\nu_c = 0.01$ GHz and $\nu_c = 1$ GHz, and for $\rho' = 65$ mm and $\rho' = 61$ mm. We see that for the lower collisionality case, the electromagnetic disturbance propagates without significant damping around the plasma cylinder, whereas for higher collisionality, the wave is attenuated by the time it propagates a distance of about a quarter of its circumference. When the magnetic line source is placed closer to the plasma, we see that the coupling

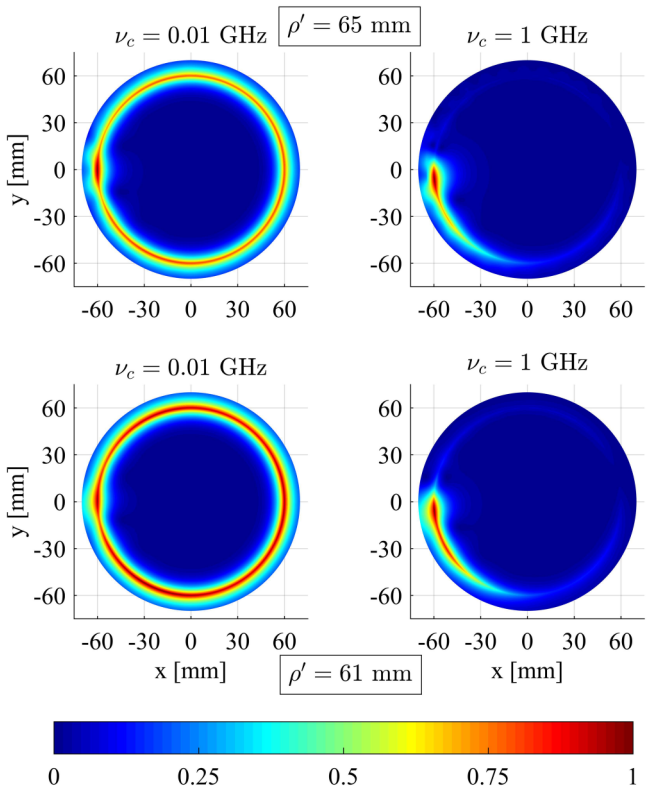

FIG. 4. Calculated magnitude of the normalized magnetic field at $f = 0.78f_p = 4.914$ GHz, for $f_b = 0.24f_p = 1.512$ GHz, $\varepsilon_c = 1$ with $\rho' = 65$ mm, and $\rho' = 61$ mm.

to the surface wave is more efficient. To confirm the findings of this analytical model, we have performed simulations using CST Microwave Studio (MWS), with the magnetic line source generated by a small loop antenna and periodic boundary conditions along the z-axis. The resulting root-mean-square (RMS) of the magnetic field is shown in Fig. 5 for the $\rho' = 65$ mm case. The CST results are seen to be in good agreement with those of the analytical model.

In addition to the locus of intense activity seen in Fig. 3 below the plasma frequency, there is also another strongly active region above the plasma frequency, particularly when $\rho' = 61$ mm, i.e., when the source is almost located at the air-plasma boundary. For these plasma conditions, this activity lies in a frequency range bounded by the lower and upper extraordinary mode (or, X-mode)[38] for propagation along a direction perpendicular to the magnetic field in the bulk plasma. Relevant to the topological classification, this interfacial disturbance lies within the bandgap for the propagation of such X-modes, which have the wave magnetic field parallel to imposed external magnetic bias. The plasma conditions also place us in an overdense regime, with $f_p > f_b$, and in a region where the magnetized plasma is classified as a Weyl semimetal.[39] In this regime, there is a single degenerate (Weyl) point

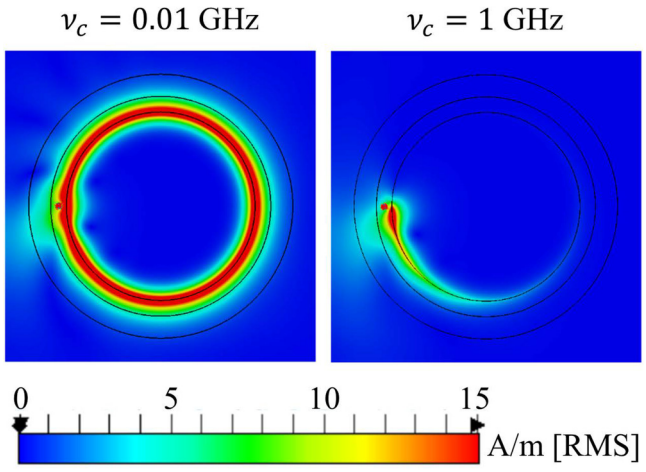

FIG. 5. Simulated magnetic field (RMS value) using CST MWS at $f = 0.78f_p = 4.914$ GHz, for $f_b = 0.24f_p = 1.512$ GHz, $\varepsilon_c = 1$ (air), and various collision frequencies, for $\rho' = 65$ mm.

located where the electrostatic and left circularly polarized mode dispersion surfaces cross, triggering a topological phase transition.[28] The significance of the resulting non-trivial topological phase is discussed later in Sec. IV.

The resulting normalized power for this higher frequency mode with $f/f_p = 1.29$ and $f_b/f_p = 0.8$ is shown in Fig. 6 for values of the collision frequency, $\nu_c = 0.01$ GHz and $\nu_c = 1$ GHz, and for $\rho' = 65$ mm and $\rho' = 61$ mm. As noted above, the value of the merit function for $\rho' = 61$ mm is much larger than that of $\rho' = 65$ mm, since the source's distance to the magnetized plasma is $d \approx 0.03\lambda = 1$ mm vs $d \approx 0.14\lambda = 5$ mm for $\rho' = 65$ mm case. However, an examination of the normalized power, despite the strength of the merit functions for these high frequency modes, indicates that these waves are not surface waves. These waves appear to be radiating into the un-ionized surrounding. In the section below, we consider the addition of a metal cladding to prevent these surface waves from coupling into radiative modes. From a topological perspective, the addition of the metal cladding introduces a material that shares a common bandgap with the bulk magnetized plasma. Below, we examine the impact of this metal cladding on this higher frequency mode, as well as the lower frequency disturbances.

C. Cladding with negative permittivity medium as a mirror

Here, we consider the addition of a metal cladding (for $\rho > r_c$) with negative permittivity, i.e., $\varepsilon = -10$ and its impact on both the low and high frequency disturbances. Again, we examine two cases: (a) $\rho' = 65$ mm and $r_c = 70$, and, (b) $\rho' = 61$ mm and $r_c = 62$ mm. The respective merit functions are shown in Fig. 7. The resulting surface waves are discussed below.

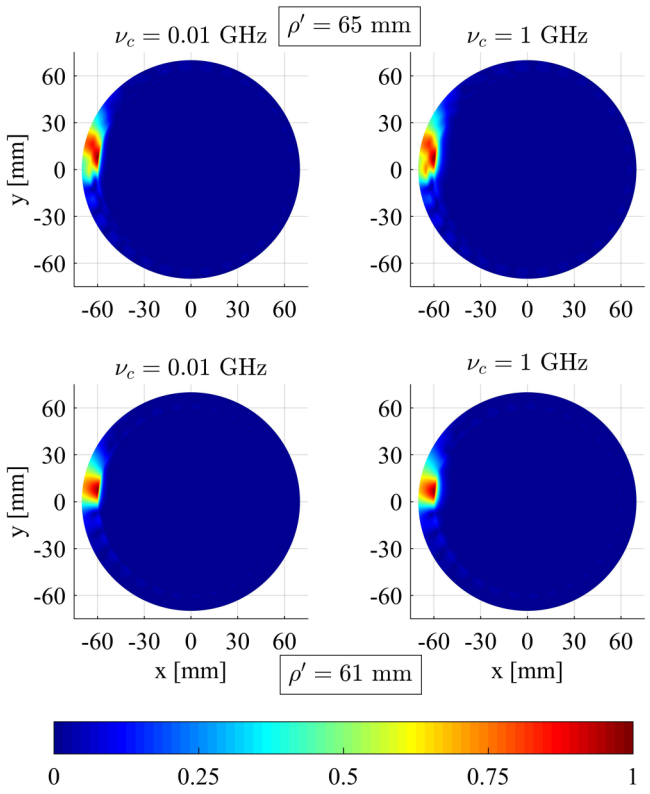

FIG. 6. Calculated magnitude of the normalized magnetic field at $f = 1.29f_p = 8.127$ GHz, for $f_b = 0.8f_p = 5.04$ GHz, $\varepsilon_c = 1$ with $\rho' = 65$ mm and $\rho' = 61$ mm.

1. Non-topological surface waves

Figure 7 reveals that for the low frequency disturbance, we see a behavior similar to that of Fig. 3(a), with the persistence of a low frequency mode in the vicinity of $f_r^+ = f_r + f_p/2$. The normalized power for the case of $f/f_p = 0.78$ and $f_b/f_p = 0.24$ is shown in Fig. 8 for both magnetic line source locations. When $\rho' = 65$ mm, the distance between the magnetic line source and magnetized plasma is $d = 5$ mm $\approx 0.14\lambda$, and the gap between the magnetized plasma rod and the metal cladding (with $\varepsilon = -10$) is $g = 10$ mm $\approx 0.28\lambda$, enabling the unidirectional magnetoplasmon waves to be excited at the plasma-vacuum boundary. Despite the strongly confined propagation, again, these low frequency interfacial modes are not topologically protected. When the magnetic line source position relative to the plasma and gap thickness is significantly reduced ($d = 1$ mm $\approx 0.03\lambda$ and $g = 2$ mm $\approx 0.06\lambda$, respectively), we see that no surface waves are excited. In this case, the magnetic line source is sandwiched between two mirrors ($\varepsilon_c < 0$ and $\Re(\varepsilon_t) < 0$), and accordingly, the fields will be trapped within a small region near the source.

Again, for this low frequency mode, we have also performed simulations using CST for the propagating case shown in Fig. 8. The resulting root-mean-square (RMS) of the magnetic field is

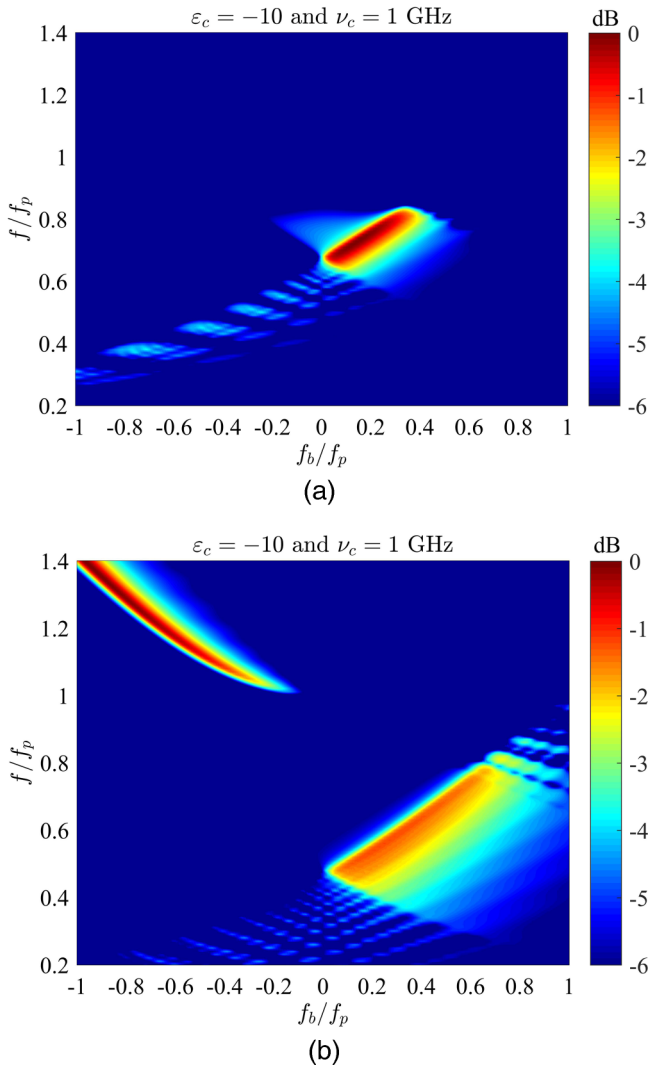

FIG. 7. The merit function normalized to its maximum in dB, F_{dB}^{norm}, vs f_b/f_p and f/f_p for $\varepsilon_c = -10$ and $\nu_c = 1$ GHz: (a) $\rho' = 65$ mm and $r_c = 70$ mm and (b) $\rho' = 61$ mm and $r_c = 62$ mm.

shown in Fig. 9 for the case of $\rho' = 65$ mm and $r_c = 70$ mm. The CST results are seen to be in good agreement with the analytical analysis and confirm the existence of such a wave that is highly confined to the plasma-un-ionized gas interface. In both cases (i.e., the analytical scattering model and CST simulations), low collisionality conditions show that the interfacial wave propagates all the way around, returning to its initial location with very little dissipation. As expected, in the case where the collisional damping is comparable to the field frequency, we see that the disturbance makes it barely halfway around the cylindrical plasma.

As mentioned previously, although the unidirectional magnetoplasmons are strictly not topologically protected, they do appear to be immune to back-scattering from defects such as surface

protrusions containing sharp corners. To illustrate this, we have performed a simulation (assuming low plasma collisionality) with a defined sharp rectangular protrusion in the cladding, parameterized with dimensions $D_x = 40$ mm and $D_y = 26.57$ mm, as shown in the left schematic in Fig. 10. The thickness of the air gap is 10 mm. A snapshot in time of the magnitude of the resulting magnetic field is also shown in Fig. 10. We see that the highly confined surface waves propagate around the protrusion, confirming the existence of a robust surface wave.

2. Topological surface waves

We now turn our attention to the second, high frequency active region seen in the merit function for the case of $\rho' = 61$ mm and $r_c = 62$ mm. It is noteworthy that this mode appears to be inactive in the $\rho' = 65$ mm and $r_c = 70$ mm case, based on the merit function in Fig. 7. The normalized power for $f/f_p = 1.29$ and $f_b/f_p = 0.8$ is shown in Fig. 11. Despite the difference in merit functions, these two cases have seemingly similar field distributions. The reason for this is that the merit function is required to be maximum at the edge of the plasma-air boundary. A close inspection of the fields reveals that for the case of a larger distance

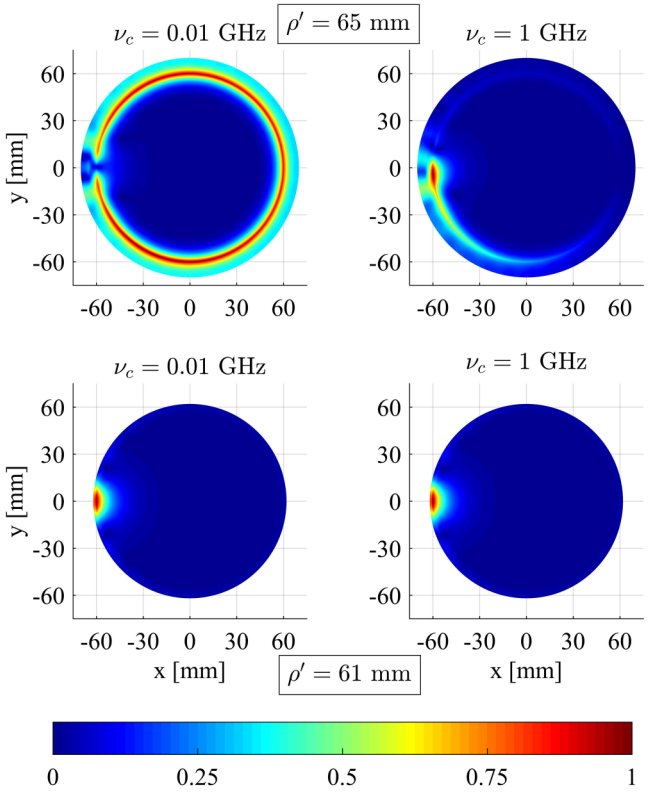

FIG. 8. Calculated magnitude of the normalized magnetic field at $f = 0.78 f_p = 4.914$ GHz, for $f_b/f_p = 0.24$, $\varepsilon_c = -10$, and various collision frequencies.

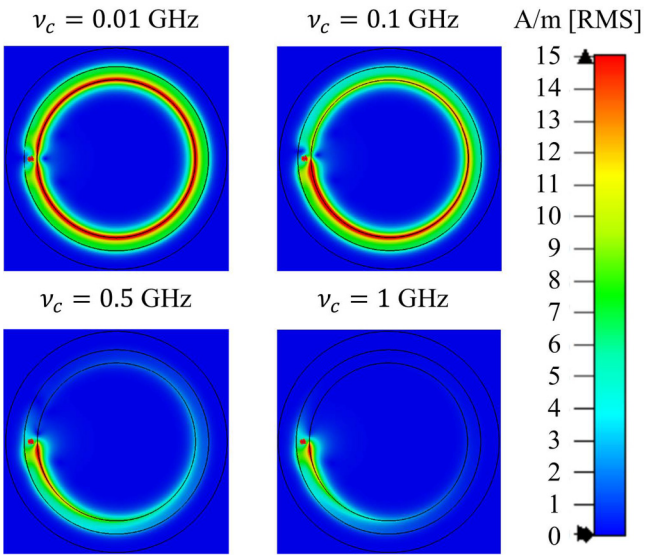

FIG. 9. Simulated magnetic field (RMS value) using CST MWS at $f = 0.78 f_p = 4.914$ GHz, for $f_b/f_p = 0.24$, $\varepsilon_c = -10$, and various collision frequencies, for the case of $\rho' = 65$ mm and $r_c = 70$ mm.

and gap, the fields are mostly concentrated near the metallic cladding and not the edge of the plasma.

We have performed CST simulations of these conditions as a further confirmation of these findings. The resulting RMS of the magnetic field is shown in Fig. 12 for the case of $\rho' = 61$ mm and $r_c = 62$ mm. The CST results are in good agreement with the analytical model results further confirming the existence of a wave that is highly confined to the plasma-mirror interface. The low collisionality case shows that the interfacial wave propagates all the way around the plasma rod, returning to its initial location with very little dissipation. We can also see that the disturbance makes it

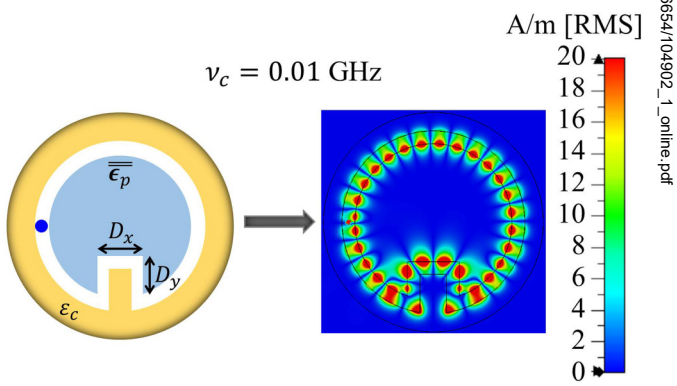

FIG. 10. A snapshot of the magnetic field distribution at $f = 0.78 f_p = 4.914$ GHz, for $f_b/f_p = 0.24$ in the case of the presence of a square defect in the bulk magnetized plasma, with $D_x = 40$ mm and $D_y = 26.57$ mm.

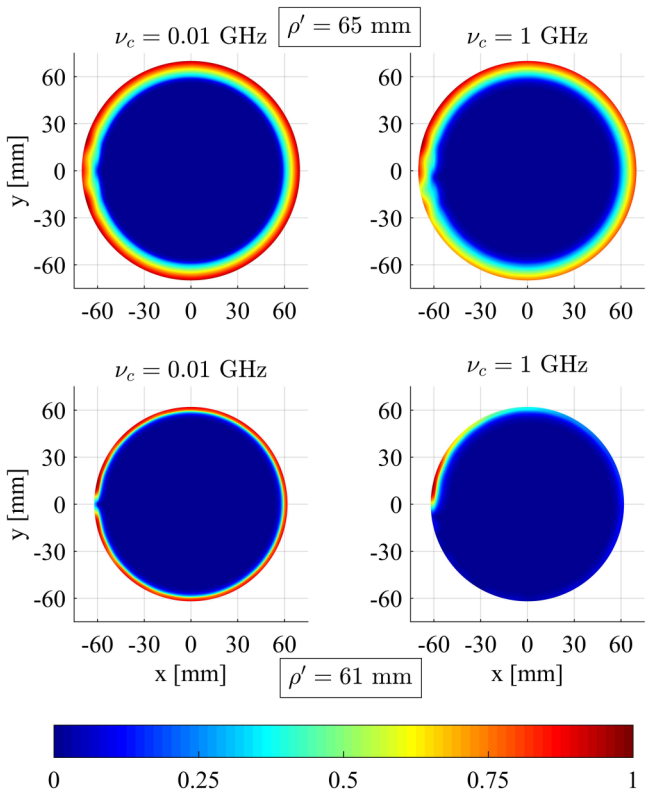

FIG. 11. Calculated magnitude of the normalized magnetic field at $f = 1.29f_p = 8.127$ GHz, for $f_b = 0.8f_p = 5.04$ GHz, $\varepsilon_c = -10$ with $\rho' = 65$ mm and $\rho' = 61$, for $\nu_c = 0.01$ GHz and $\nu_c = 1$ GHz.

barely halfway around the cylindrical plasma for higher collisional damping. As discussed in Sec. IV, this configuration and magnetized plasma/metal cladding interface condition constitute a topologically protected state that results in its robust, unidirectional, interface persistence. A topological classification requires an assessment of the gap Chern number of the bulk magnetized plasma. As there is only one identified interfacial mode over this frequency range, this gap Chern number is expected to have a unity value, as the topologically trivial mirror presents a gap Chern number of zero.

For this strongly unidirectional mode, we again have performed a simulation with a defined rectangular protrusion in the cladding, but with dimensions $D_x = 20$ mm and $D_y = 29.16$ mm. The thickness of the air gap around the protrusion is set at 2 mm. A snapshot in time of the magnitude of the resulting magnetic field is shown in Fig. 13. It is apparent that the highly confined surface waves propagate around the defect, consistent with the existence of a robust, topological surface wave.

3. Interfacial states at boundaries of effective magnetized bulk plasmas

In the above section, we describe the identification of conditions for non-topological and topological states at the interface of a

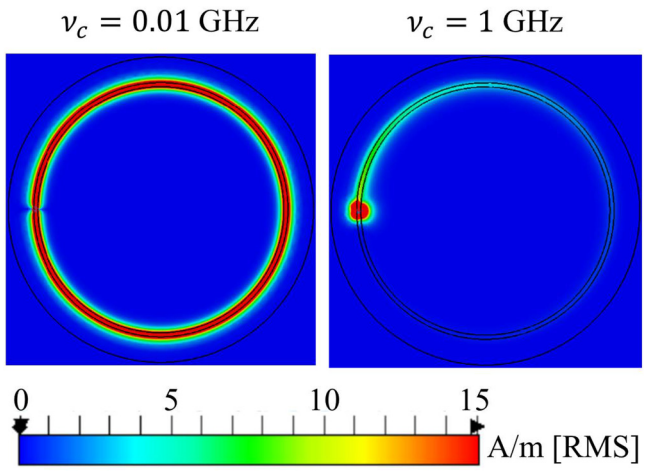

FIG. 12. Simulated magnetic field (RMS value) using CST MWS at $f = 1.29f_p = 8.127$ GHz, for $f_b = 0.8f_p = 5.04$, $\varepsilon_c = -10$, and various collision frequencies, for the case of $\rho' = 61$ mm and $r_c = 62$ mm.

bulk magnetized plasma boundary. In practice, such states may be difficult to excite and probe, particularly so if the plasma is confined by a sealed dielectric envelope to support vacuum conditions. Furthermore, such plasmas are not necessarily uniform in their properties, and in some cases, topological interfacial waves are seen to propagate with fields concentrated within the plasma gradient regions[40] spanning across two different topological plasma phases.[28] While it is challenging in practice to generate a true, uniform bulk magnetized plasma, one can assemble an effective bulk magnetized plasma with a collection of sub-wavelength plasma elements. Such an assembly can present an "effective" bulk medium, i.e., behaves as a magnetized plasma metamaterial. In this regard, we propose to construct such a uniform effective bulk magnetized plasma using a densely packed array of magnetized plasma discharge tubes. Here, in a particular example, we assemble an effective bulk magnetized plasma cylinder using 37 smaller uniform plasma columns. These columns are taken to be 15 mm in diameter, and are assumed to have similar plasma diameters and properties (electron number density and collision frequency) to those which we have used previously to construct plasma-based metamaterials and photonic crystals.[41–46] The merit function for identifying the edge states in this effective bulk medium configuration is shown in Fig. 14, where the surrounding cladding medium is considered to be a perfect electric conductor (PEC).

For the case of the lower frequency non-topological magnetoplasmon waves, the RMS of the simulated wave magnetic field for such an effective bulk plasma cylinder is shown in Fig. 15. To obtain the performance of the aforementioned magnetized bulk plasma at the same frequency of operation as the uniform bulk plasma examples, $f = 4.914$ GHz, the cylindrical element plasma and cyclotron frequencies have been increased to $f_p^{eff} = 7$ GHz and $f_b^{eff} = 1.97$ GHz, respectively. We see that there is an interfacial state propagating between the plasma cylinders and the PEC for

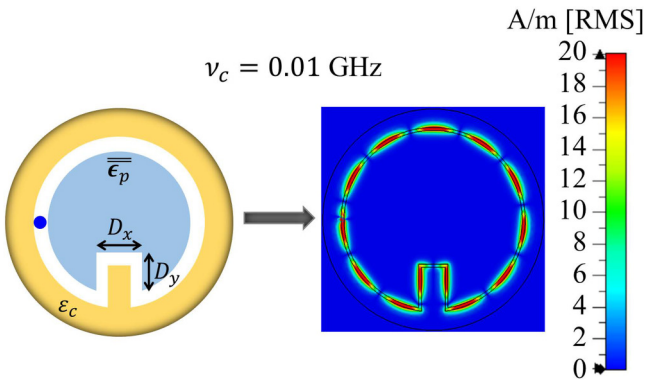

FIG. 13. A snapshot of the magnetic field distribution at $f = 1.29 f_p = 8.127$ GHz, for $f_b/f_p = 0.8$ in the case of the presence of a square defect in the bulk magnetized plasma, with $D_x = 20$ mm and $D_y = 29.16$ mm.

conditions of relatively low collisionality. In yet another example, to illustrate the utility of this EM-based approach, we apply this to a chain of these metamaterial cylinders constructed from these effective bulk (and now moderately collisional) magnetized plasmas cylinders. The assemblies are coupled through openings in the PEC cladding with the source located at the 9-o'clock position on the far-left cylinder. The simulated magnetic wave fields for such a chain is shown in Fig. 16. The fields rotate in a counter-clockwise fashion, and mimic a chain of rotating carousels, with wave propagation predominantly coupling on the lower half of adjacent metamaterial cylinders.

For the case of the higher frequency topological surface wave seen in Fig. 14, the RMS of the simulated wave magnetic field is

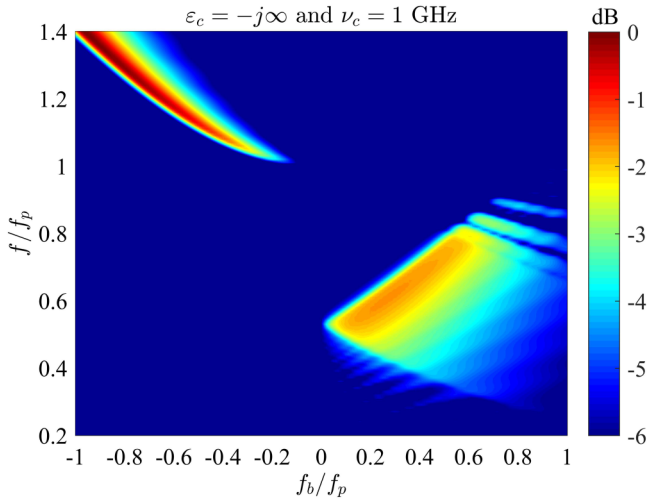

FIG. 14. The merit function normalized to its maximum in dB, F_{dB}^{norm}, vs f_b/f_p and f/f_p, for $\varepsilon_c = -j\infty$ (PEC as the surrounding medium) and $\nu_c = 1$ GHz.

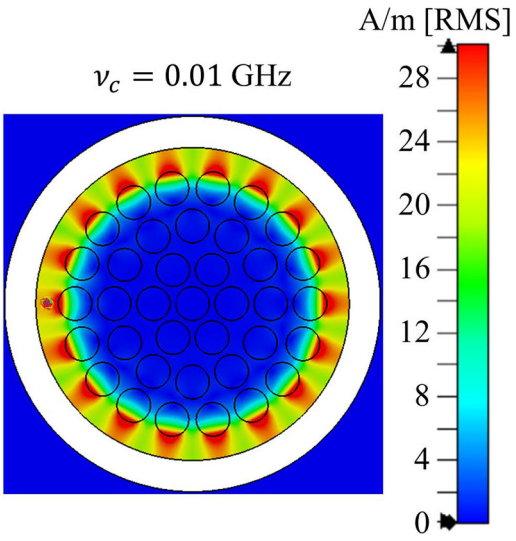

FIG. 15. Simulated magnetic field (RMS value) of the proposed realization of the magnetized plasma using CST MWS at $f = 0.7 f_p^{eff} = 4.914$ GHz, for $f_b^{eff}/f_p^{eff} = 0.28$ and $\nu_c = 0.01$ GHz.

shown in Fig. 17. For this simulation, we have again taken the cladding to be a PEC and individual plasma cylinder densities are such that $f/f_p^{eff} = 1.29$ and $f_b^{eff}/f_p^{eff} = 0.8$. We see that there is a persistent interfacial state propagating between the effective bulk plasma and the PEC for a low collisionality condition. Again, we apply this to a chain of these moderately collisional metamaterial magnetized plasma cylinders similar to that of the low frequency case discussed above. The simulated magnetic wave fields for such a chain is shown in Fig. 18. The fields rotate in a clockwise fashion, and the resulting fields again mimic a chain of rotating carousels, with wave propagation coupling predominantly on the upper half of adjacent metamaterial cylinders.

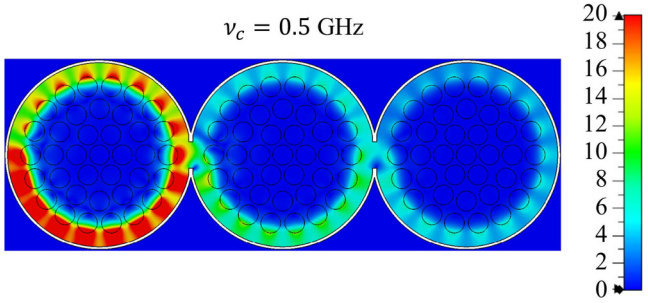

FIG. 16. The RMS of the magnetic field simulated using CST MWS for a chain of carousels at $f = 0.7 f_p^{eff} = 4.914$ GHz, for $f_b^{eff}/f_p^{eff} = 0.28$ and $\nu_c = 0.5$ GHz.

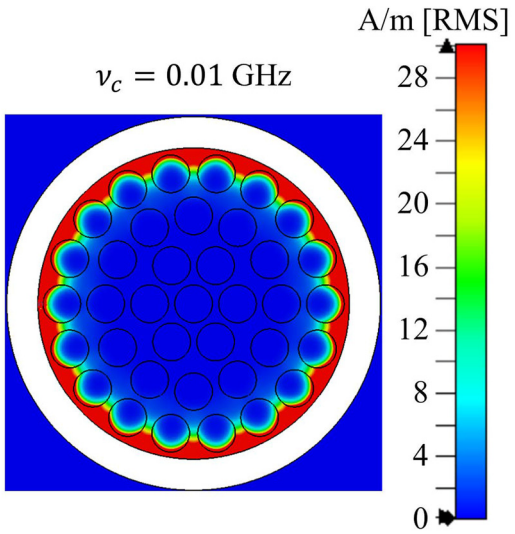

FIG. 17. Simulated magnetic field (RMS value) of the proposed realization of the magnetized plasma using CST MWS at $f = 1.29 f_p^{eff} = 8.127$ GHz, for $f_b^{eff} = 0.8 f_p^{eff} = 5.04$ GHz and $\nu_c = 0.01$ GHz.

IV. TOPOLOGICAL ORIGIN AND CLASSIFICATION

In the sections above, we have shown that the proposed analytical analysis enables us to find possible interfacial surface waves associated with gaseous plasmonic systems, topological or not in their designation. Interfacial states associated with magnetized plasmonic systems have received significant attention,[31,47–49] particularly those that are traceable to topological properties of the bulk plasma.[28,30,50–52] As mentioned earlier, the topological classification of bulk bands are associated with the band Chern number, which can be computed by integrating the Berry curvature over the bulk band dispersion in reciprocal wavelength (wavenumber) space.[29,53] However, unlike a periodic medium, a continuous medium such as a gaseous plasma described by a local Drude model does not have a compacted Brillouin zone as wavenumbers extend to infinite values. As a result, this may give rise to non-integer band Chern numbers. Several recent papers describe methods of addressing this by restricting the range of wavevector integration,[12,28,29,40] sometimes with rather *ad hoc* limits. It is noteworthy here, however, that when used in our analytical EM model, the local Drude model does indeed yield the robust unidirectional topological states, without requiring any further assumptions. Clearly, the theoretical determination of band Chern numbers for magnetized gaseous plasmas still requires further study. In this regard, a rigorous theoretical treatment for computing Chern numbers in continuous media was recently proposed by Qin and Fu.[54]

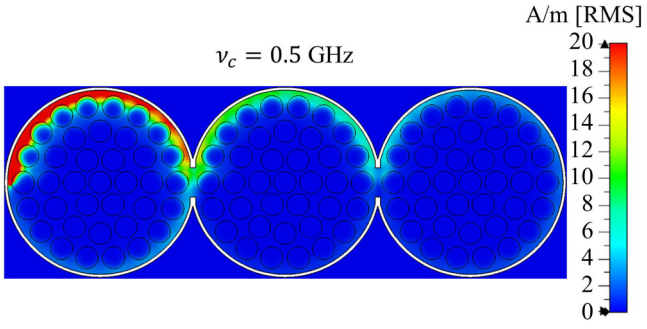

FIG. 18. The RMS of the magnetic field simulated using CST MWS for a chain of carousels at $f = 1.29 f_p^{eff} = 8.127$ GHz, for $f_b^{eff} = 0.8 f_p^{eff} = 5.04$ and $\nu_c = 0.5$ GHz.

Band Chern numbers change only when the system undergoes a topological phase transformation. Neglecting ion motion, a cold, magnetized plasma has four active dispersion surfaces[38] which, for wave propagation purely transverse to the imposed magnetic field ($k_\parallel = 0$), reduce to the lower and upper X-mode, the O-mode, and a zero-frequency ($\omega = 0$) mode. Figure 19(a) plots the two X-modes for plasma parameters corresponding to Fig. 11. The four bands when $k_\parallel = 0$ evolve into the upper and lower Right Circular Polarized (RCP) modes, the LCP mode, and the Langmuir (electrostatic) mode as the propagation vector rotates ($k_\parallel > 0$) to eventually become parallel to the external magnetic field, with $k_\perp = 0$ [see the four bands plotted in Fig. 19(b) for conditions of Fig. 11]. For our overdense conditions, we see from Fig. 19(b) that there is a single (inner) Weyl point degeneracy where the Langmuir and LCP mode cross, giving rise to a source of Berry curvature (or a momentum space monopole).[24] The Weyl point crossing occurs at a component wavenumber $k_\parallel = k^+$, where

$$k^+ = \frac{\omega_p/c}{\sqrt{1+\omega_p/\omega_b}}. \tag{18}$$

As shown by Fu and Qin,[28] Weyl degeneracies in a cold magnetized plasma delineate three distinctly different topological magnetized plasma phases that span across the dispersion space characterized by their corresponding sets of band Chern numbers. Disturbances with $k_\parallel = 0$, as is the case here, belong to a topological phase with band Chern numbers $(C_1, C_2, C_3, C_4) = (-1, 2, 0, -1)$ for the zero-frequency, lower X-mode, O-mode, and upper X-mode, respectively.[28] We have confirmed these Chern numbers using the method outlined by Hanson *et al.*[29] with a spatial cut-off ($k_{max} = 10\omega_b/c$) of the plasma frequency.[12,55] The X-mode gap Chern number is, therefore, $C_{2,4} = 1$. An interface consisting of this magnetized plasma with a trivial gapped medium such as a metal predicts the existence of a single topological edge state, as we have identified using our analytical EM model. This edge state is also shown in Fig. 19(a), computed using the dispersion relation for magnetoplasmon waves in the Voigt configuration, as developed by Davoyan and Engheta.[56]

With plasma properties constant, a rotation of the direction of propagation by increasing $k_\parallel$ will sample a second topological phase with Chern numbers $(-1, 1, 1, -1)$,[28] when the propagation angle relative to the imposed magnetic field is such that $k_\parallel \geq k^+$. A third topological phase transition may occur in underdense

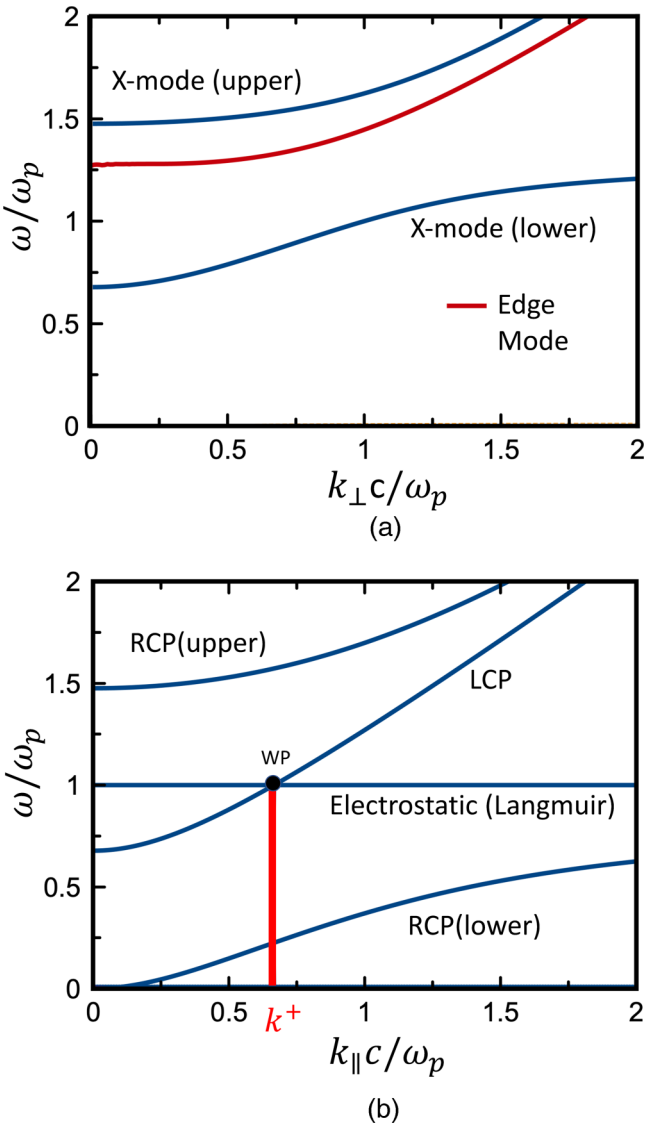

FIG. 19. Cold plasma dispersion for (a) $k_\parallel = 0$ (only the lower and upper X-modes), with edge-state shown in red. (b) $k_\perp = 0$ (non-zero modes). The Weyl point (WP) appears at k^+. (a) $k_\parallel = 0$. (b) $k_\perp = 0$.

plasmas due to the emergence of a second (upper) Weyl point[28] at

$$k^- = \frac{\omega_p/c}{\sqrt{1-\omega_p/\omega_b}}. \tag{19}$$

It is noteworthy that we do not access these two other topological phases in our current studies because of our 2D geometry as it requires a component of the propagation along the direction of the bias. A future study seeks to extend the analytical model to three dimensions (3D) to be able to further examine this rich topological space and enable designs of plasma metamaterials that may afford experimental validations. With a 3D model, other scenarios include more complex systems such as interfaces between plasmas of different plasma densities, which have been explored recently by Parker *et al.*[40] and Fu and Qin.[28] Rather exotic Fermi-arc like edge states have been described connecting the corresponding Weyl degeneracies of the two adjacent plasma mediums. While single non-uniform bulk cylindrical plasma can present such an interface with the magnetic field aligned with the cylinder axis, a 3D analytical model will facilitate identifying conditions that may enable the construction of such effective bulk plasma interfaces using plasma arrays to excite these exotic topological edge states.

V. SUMMARY

In this paper, we have presented an approach to identify the existence of topological as well as non-topological waves confined to the boundary between a magnetized plasma and a topologically trivial medium, such as air or a gapped metal. The approach is based on the analytical solution of electromagnetic field scattering, originating from an excited magnetic line source located at the interface of a gyrotropic, magnetized plasma, and an un-ionized gas. A merit function is introduced for quantification of the power concentrated along a desired path at the boundary. The analytical formalism allows us to rapidly survey the design space to identify conditions in which robust interfacial states, topological and non-topological, may be supported. We show that the dispersion of the topological state identified is consistent with its classification based on computed Chern numbers using Barry phase concepts and the ensuing topological phases are connected to the Weyl degeneracy present under the examined plasma conditions. Examples are provided where we have applied this EM approach to both bulk and effective bulk magnetized plasma structures and have confirmed that magnetized plasma metamaterials can be constructed from experimentally realizable plasma discharge tubes. We believe that such an approach, stemming from an applied engineering perspective, may facilitate the design of practical devices incorporating magnetized plasma structures.

ACKNOWLEDGMENTS

This research is supported by an Air Force Office of Scientific Research Multi-University Research Initiative (MURI), Grant No. FA9550-21-1-0244, with Dr. Mitat Birkan as program manager. The authors would like to thank the reviewers for their comments, particularly the one reviewer who's persistence in recommending that we expand our discussion on the connection of this modeling to the topological underpinnings, which resulted in a much improved manuscript.

AUTHOR DECLARATIONS

Conflict of Interest

The authors have no conflicts to disclose.

Author Contributions

Hossein Mehrpour Bernety: Conceptualization (equal); Data curation (equal); Formal analysis (equal); Investigation (equal); Methodology (equal); Software (equal); Supervision (equal); Validation (equal); Visualization (equal); Writing – original draft (equal); Writing – review & editing (equal). **Mark A. Cappelli:** Conceptualization (equal); Formal analysis (equal); Funding acquisition (equal); Investigation (equal); Methodology (equal); Project administration (equal); Resources (equal); Supervision (equal); Validation (equal); Visualization (equal); Writing – original draft (equal); Writing – review & editing (equal).

DATA AVAILABILITY

The data that support the findings of this study are available from the corresponding author upon reasonable request.

APPENDIX

Here, we present the mathematical formulation to determine the unknown coefficients of the electromagnetic scattering problem, i.e., a_n, B_n, C_n, and d_n. In doing so, we apply the four boundary conditions as follows:

$$H_z^p|_{\rho=r_p} = [H_z^a + H_z^i]|_{\rho=r_p}, \tag{A1}$$

$$E_\varphi^p|_{\rho=r_p} = [E_\varphi^a + E_\varphi^i]|_{\rho=r_p}, \tag{A2}$$

$$H_z^c|_{\rho=r_c} = [H_z^a + H_z^i]|_{\rho=r_c}, \tag{A3}$$

$$E_\varphi^c|_{\rho=r_c} = [E_\varphi^a + E_\varphi^i]|_{\rho=r_c}. \tag{A4}$$

For each value of n, there exists the matrix equation

$$\begin{bmatrix} 0 & J_n(k_0 r_p) & Y_n(k_0 r_p) & -J_n(k_p r_p) \\ 0 & J_n'(k_0 r_p) & Y_n'(k_0 r_p) & X \\ H_n^{(2)}(k_c r_c) & -J_n(k_0 r_c) & -Y_n(k_0 r_c) & 0 \\ H_n^{(2)'}(k_c r_c)/\varepsilon_c & -J_n'(k_0 r_c) & -Y_n'(k_0 r_c) & 0 \end{bmatrix} \cdot \begin{bmatrix} a_n \\ B_n \\ C_n \\ d_n \end{bmatrix} = \begin{bmatrix} -H_0 J_n(k_0 r_p) H_n^{(2)}(k_0 \rho') \\ -H_0 J_n'(k_0 r_p) H_n^{(2)}(k_0 \rho') \\ H_0 J_n(k_0 \rho') H_n^{(2)}(k_0 r_c) \\ H_0 J_n(k_0 \rho') H_n^{(2)'}(k_0 r_c) \end{bmatrix}, \tag{A5}$$

wherein

$$X = -\frac{n}{r_p \varepsilon_p'} J_n(k_p r_p) - \frac{1}{\varepsilon_p} J_n'(k_p r_p) \tag{A6}$$

and the derivatives can be calculated as[5]

$$Z_n'(\alpha x) = \frac{\partial Z_n(\alpha x)}{\partial x} = \alpha Z_{n-1}(\alpha x) - \frac{n}{x} Z_n(\alpha x), \tag{A7}$$

wherein Z_n can be a Bessel function (J_n or Y_n) or a Hankel function ($H_n^{(2)}$).[5]

REFERENCES

[1] A. V. Oppenheim, A. S. Willsky, S. H. Nawab, G. M. Hernández *et al. Signals & Systems* (Pearson Educación, 1997).
[2] H. Li, S. Yin, and A. Alù, "Nonreciprocity and faraday rotation at time interfaces," Phys. Rev. Lett. **128**, 173901 (2022).
[3] C. Caloz, A. Alu, S. Tretyakov, D. Sounas, K. Achouri, and Z.-L. Deck-Léger, "Electromagnetic nonreciprocity," Phys. Rev. Appl. **10**, 047001 (2018).
[4] J. R. Carson, "Reciprocal theorems in radio communication," Proc. Inst. Radio Eng. **17**, 952–956 (1929).
[5] C. A. Balanis, *Advanced Engineering Electromagnetics* (John Wiley & Sons, 2012).
[6] A. Kord, D. L. Sounas, and A. Alu, "Microwave nonreciprocity," Proc. IEEE **108**, 1728–1758 (2020).
[7] G. D'Aguanno, D. L. Sounas, H. M. Saied, and A. Alù, "Nonlinearity-based circulator," Appl. Phys. Lett. **114**, 181102 (2019).
[8] A. Mock, D. Sounas, and A. Alu, "Magnet-free circulator based on spatiotemporal modulation of photonic crystal defect cavities," ACS Photonics **6**, 2056–2066 (2019).
[9] J. Wang, J. F. Herrmann, J. D. Witmer, A. H. Safavi-Naeini, and S. Fan, "Photonic modal circulator using temporal refractive-index modulation with spatial inversion symmetry," Phys. Rev. Lett. **126**, 193901 (2021).
[10] A. M. Holmes, M. Sabbaghi, and G. W. Hanson, "Experimental realization of topologically protected unidirectional surface magnon polaritons on ceramic yig ferrites," Phys. Rev. B **104**, 214433 (2021).
[11] A. Okamoto, R. Shindou, and S. Murakami, "Berry curvature for coupled waves of magnons and electromagnetic waves," Phys. Rev. B **102**, 064419 (2020).
[12] M. G. Silveirinha, "Chern invariants for continuous media," Phys. Rev. B **92**, 125153 (2015).
[13] Y. Liang, S. Pakniyat, Y. Xiang, J. Chen, F. Shi, G. W. Hanson, and C. Cen, "Tunable unidirectional surface plasmon polaritons at the interface between gyrotropic and isotropic conductors," Optica **8**, 952–959 (2021).
[14] Z. Wang, Y. Chong, J. D. Joannopoulos, and M. Soljačić, "Observation of unidirectional backscattering-immune topological electromagnetic states," Nature **461**, 772–775 (2009).
[15] A. B. Khanikaev, S. Hossein Mousavi, W.-K. Tse, M. Kargarian, A. H. MacDonald, and G. Shvets, "Photonic topological insulators," Nat. Mater. **12**, 233–239 (2013).
[16] S. A. H. Gangaraj, M. G. Silveirinha, and G. W. Hanson, "Berry phase, berry connection, and chern number for a continuum bianisotropic material from a classical electromagnetics perspective," IEEE J. Multiscale Multiphys. Comput. Tech. **2**, 3–17 (2017).
[17] D. E. Fernandes and M. G. Silveirinha, "Topological origin of electromagnetic energy sinks," Phys. Rev. Appl. **12**, 014021 (2019).
[18] T. Ozawa, H. M. Price, A. Amo, N. Goldman, M. Hafezi, L. Lu, M. C. Rechtsman, D. Schuster, J. Simon, O. Zilberberg, and I. Carusotto, "Topological photonics," Rev. Mod. Phys. **91**, 015006 (2019).
[19] L. Lu, J. D. Joannopoulos, and M. Soljačić, "Topological photonics," Nat. Photonics **8**, 821–829 (2014).
[20] M. C. Rechtsman, J. M. Zeuner, Y. Plotnik, Y. Lumer, D. Podolsky, F. Dreisow, S. Nolte, M. Segev, and A. Szameit, "Photonic floquet topological insulators," Nature **496**, 196–200 (2013).
[21] Z. Wang, Y. Chong, J. D. Joannopoulos, and M. Soljačić, "Reflection-free one-way edge modes in a gyromagnetic photonic crystal," Phys. Rev. Lett. **100**, 013905 (2008).
[22] Z. Yu, G. Veronis, Z. Wang, and S. Fan, "One-way electromagnetic waveguide formed at the interface between a plasmonic metal under a static magnetic field and a photonic crystal," Phys. Rev. Lett. **100**, 023902 (2008).
[23] B. Yang, M. Lawrence, W. Gao, Q. Guo, and S. Zhang, "One-way helical electromagnetic wave propagation supported by magnetized plasma," Sci. Rep. **6**, 21461 (2016).

[24]W. Gao, M. Lawrence, B. Yang, F. Liu, F. Fang, B. Béri, J. Li, and S. Zhang, "Topological photonic phase in chiral hyperbolic metamaterials," Phys. Rev. Lett. **114**, 037402 (2015).
[25]S. A. Hassani Gangaraj, A. Nemilentsau, and G. W. Hanson, "The effects of three-dimensional defects on one-way surface plasmon propagation for photonic topological insulators comprised of continuum media," Sci. Rep. **6**, 1–10 (2016).
[26]S. A. H. Gangaraj, G. W. Hanson, M. G. Silveirinha, K. Shastri, M. Antezza, and F. Monticone, "Unidirectional and diffractionless surface plasmon polaritons on three-dimensional nonreciprocal plasmonic platforms," Phys. Rev. B **99**, 245414 (2019).
[27]S. A. H. Gangaraj and F. Monticone, "Physical violations of the bulk-edge correspondence in topological electromagnetics," Phys. Rev. Lett. **124**, 153901 (2020).
[28]Y. Fu and H. Qin, "Topological phases and bulk-edge correspondence of magnetized cold plasmas," Nat. Commun. **12**, 3924 (2021).
[29]G. W. Hanson, S. Gangaraj, and A. Nemilentsau, "Notes on photonic topological insulators and scattering-protected edge states-a brief introduction," arXiv:1602.02425 (2016).
[30]K. Shastri, M. I. Abdelrahman, and F. Monticone, "Nonreciprocal and topological plasmonics," in *Photonics* (MDPI, 2021), Vol. 8, p. 133.
[31]S. A. H. Gangaraj and F. Monticone, "Do truly unidirectional surface plasmon-polaritons exist?," Optica **6**, 1158–1165 (2019).
[32]S. Seshadri, "Excitation of surface waves on a perfectly conducting screen covered with anisotropic plasma," IRE Trans. Microwave Theory Tech. **10**, 573–578 (1962).
[33]A. Ishimaru, "Unidirectional waves in anisotropic media and the resolution of thethermodynamic paradox," Tech. Rep., Washington University, Seattle, 1962.
[34]P. Karimi, B. Rejaei, and A. Khavasi, "Unidirectional surface waves in bi-anisotropic media," IEEE J. Quantum Electron. **54**, 1–6 (2018).
[35]F. F. Chen, "Physics of helicon discharges," Phys. Plasmas **3**, 1783–1793 (1996).
[36]G. W. Hanson, S. A. H. Gangaraj, and A. M. Nemilentsau, "Unidirectional, defect-immune, and topologically protected electromagnetic surface waves," in *The World of Applied Electromagnetics* (Springer, 2018), pp. 569–604.
[37]S. Pakniyat, A. M. Holmes, G. W. Hanson, S. A. H. Gangaraj, M. Antezza, M. G. Silveirinha, S. Jam, and F. Monticone, "Non-reciprocal, robust surface plasmon polaritons on gyrotropic interfaces," IEEE Trans. Antennas Propag. **68**, 3718–3729 (2020).
[38]R. O. Dendy, *Plasma Dynamics* (Clarendon Press, 1990).
[39]W. Gao, B. Yang, M. Lawrence, F. Fang, B. Béri, and S. Zhang, "Photonic weyl degeneracies in magnetized plasma," Nat. Commun. **7**, 12435 (2016).
[40]J. B. Parker, J. Marston, S. M. Tobias, and Z. Zhu, "Topological gaseous plasmon polariton in realistic plasma," Phys. Rev. Lett. **124**, 195001 (2020).
[41]B. Wang and M. Cappelli, "A plasma photonic crystal bandgap device," Appl. Phys. Lett. **108**, 161101 (2016).
[42]B. Wang and M. Cappelli, "Waveguiding and bending modes in a plasma photonic crystal bandgap device," AIP Adv. **6**, 065015 (2016).
[43]B. Wang, J. Rodríguez, and M. A. Cappelli, "3D woodpile structure tunable plasma photonic crystal," Plasma Sources Sci. Technol. **28**, 02LT01 (2019).
[44]B. Wang, J. A. Rodríguez, O. Miller, and M. A. Cappelli, "Reconfigurable plasma-dielectric hybrid photonic crystal as a platform for electromagnetic wave manipulation and computing," Phys. Plasmas **28**, 043502 (2021).
[45]F. Righetti, B. Wang, and M. Cappelli, "Enhanced attenuation due to lattice resonances in a two-dimensional plasma photonic crystal," Phys. Plasmas **25**, 124502 (2018).
[46]J. A. Rodríguez, A. I. Abdalla, B. Wang, B. Lou, S. Fan, and M. A. Cappelli, "Inverse design of plasma metamaterial devices for optical computing," Phys. Rev. Appl. **16**, 014023 (2021).
[47]J. Brion, R. Wallis, A. Hartstein, and E. Burstein, "Theory of surface magnetoplasmons in semiconductors," Phys. Rev. Lett. **28**, 1455 (1972).
[48]U. K. Chettiar, A. R. Davoyan, and N. Engheta, "Hotspots from nonreciprocal surface waves," Opt. Lett. **39**, 1760–1763 (2014).
[49]L. Shen, Y. You, Z. Wang, and X. Deng, "Backscattering-immune one-way surface magnetoplasmons at terahertz frequencies," Opt. Express **23**, 950–962 (2015).
[50]D. Jin, L. Lu, Z. Wang, C. Fang, J. D. Joannopoulos, M. Soljačić, L. Fu, and N. X. Fang, "Topological magnetoplasmon," Nat. Commun. **7**, 1–10 (2016).
[51]S. A. H. Gangaraj and G. W. Hanson, "Topologically protected unidirectional surface states in biased ferrites: Duality and application to directional couplers," IEEE Antennas Wirel. Propagation Lett. **16**, 449–452 (2016).
[52]S. A. H. Gangaraj and G. W. Hanson, "Momentum-space topological effects of nonreciprocity," IEEE Antennas Wirel. Propagation Lett. **17**, 1988–1992 (2018).
[53]Y. Fu and H. Qin, "The dispersion and propagation of topological Langmuir-cyclotron waves in cold magnetized plasmas," J. Plasma Phys. **88**, 835880401 (2022).
[54]H. Qin and Y. Fu, "Topological langmuir-cyclotron wave," arXiv:2205.02381 (2022).
[55]S. Pakniyat, S. A. H. Gangaraj, and G. W. Hanson, "Chern invariants of topological continua: A self-consistent nonlocal hydrodynamic model," Phys. Rev. B **105**, 035310 (2022).
[56]A. R. Davoyan and N. Engheta, "Theory of wave propagation in magnetized near-zero-epsilon metamaterials: Evidence for one-way photonic states and magnetically switched transparency and opacity," Phys. Rev. Lett. **111**, 257401 (2013).